INTERNATIONAL JOURNAL FOR NUMERICAL METHODS IN BIOMEDICAL ENGINEERING
Int. J. Numer. Meth. Biomed. Engng. 2013; **29**:293–308

Patient-specific computational biomechanics of the brain without segmentation and meshing[‡]

Johnny Y. Zhang, Grand Roman Joldes, Adam Wittek and Karol Miller[*,†]

Intelligent Systems for Medicine Laboratory, The University of Western Australia, Crawley, WA 6009, Australia

SUMMARY

Motivated by patient-specific computational modelling in the context of image-guided brain surgery, we propose a new fuzzy mesh-free modelling framework. The method works directly on an unstructured cloud of points that do not form elements so that mesh generation is not required. Mechanical properties are assigned directly to each integration point based on fuzzy tissue classification membership functions without the need for image segmentation. Geometric integration is performed over an underlying uniform background grid. The verification example shows that, while requiring no hard segmentation and meshing, the proposed model gives, for all practical purposes, equivalent results to a finite element model. Copyright © 2012 John Wiley & Sons, Ltd.

Received 15 March 2012; Revised 24 June 2012; Accepted 20 July 2012

KEY WORDS: patient specific modelling; brain; fuzzy mesh-free algorithms; biomechanics

1. INTRODUCTION

Neurosurgical planning for image-guided interventions is typically conducted using high quality preoperative radiographic images. For a number of common procedures (such as craniotomy) significant deformations of soft tissue can be expected, which leads to severe misalignment between the positions of pathology determined from preoperative images and their actual positions [1, 2]. These intraoperative soft tissue deformations compromise the accuracy and applicability of image-guided surgery of soft organs (such as the brain). One way to overcome these limitations is to use intraoperative guidance, which relies on image-based registration between high-resolution preoperative and intraoperative images. However, purely image-based registration may introduce unrealistic deformations and wrong correspondence between features. Furthermore, intraoperative three-dimensional scanners are incompatible with conventional instruments and surgical practice and expensive in terms of capital and running cost [3]. A viable solution that has drawn interest recently is to use patient-specific biomechanical models together with sparse intraoperative information to realistically warp the preoperative image to intraoperative configurations, that is, using a computational model that reflects the intraoperative scene to predict the soft tissue deformation during surgery [4–6]. With improved soft tissue deformation compensation that ensures plausibility of the predicted displacements, intraoperative procedures can benefit from a less invasive approach and more accurate guidance. This is based on the assumption that the patient-specific biomechanical model can be generated without much effort in clinical setting.

---

[*] Correspondence to: Karol Miller, Intelligent Systems for Medicine Laboratory, The University of Western Australia, 35 Stirling Highway, Crawley, WA 6009, Australia.

[†] E-mail: kmiller@mech.uwa.edu.au

[‡] The preliminary results of this work were presented at the first meeting of ESPRC Patient-Specific Modelling Network in Swansea University, April 2011.

Over the last 5 years, the development of patient-specific models for realistic computational simulation has been gaining more attention from research groups and government funding agencies (such as the European Research Council, Engineering and Physical Sciences Research Council (UK), National Institutes of Health (US) and Australian Research Council). These individualised high-quality biomechanical models have not yet been used in clinical practice because of the tedious manual steps in the workflow from medical images to model results [7]. The majority of such biomechanical models utilise the finite element method (FEM). The steps necessary to generate finite element models for image-guided surgery are illustrated in Figure 1, left flowchart.

Segmentation stands as the first bottleneck within the workflow. To create the finite element model, each voxel has to be segmented into distinct tissue types so that surfaces can be generated, which serve as the prerequisite for mesh generation. Manual segmentation of high-resolution volumetric images is a tedious and irreproducible task, which is impractical for processing large amount of data in clinical practice. Fully automatic and unsupervised methods, while having received significant attention in the literature, are still challenging [8]. In particular, because of the relatively low resolution of medical images, artefacts such as 'partial volume effect' [9], and geometric features of cancerous tissue growth, segmentation of the pathology (tumour) often requires intensive manual input to achieve good or even acceptable results. This is certainly confirmed by the experience in our laboratory [10].

Another necessary but tedious step in the development of the patient-specific brain model is the creation of a computational grid (meshing). Nowadays, meshing of a regular geometry is a routine task. A variety of mesh generation methods are available in the literature such as Delaunay meshing [11] and Marching Cubes [12, 13]. However, because biological structures (especially pathological tissues) often have complicated geometry, generating a high quality mesh for such structures still presents considerable challenges. Many algorithms are now available for fast and accurate automatic tetrahedral mesh generation, but not for automatic hexahedral mesh generation [14]. Unfortunately, the linear tetrahedral element exhibits volumetric locking [15, 16], especially in case of soft tissues such as the brain, which are modelled as almost incompressible materials [6, 17, 18]. Automatic hexahedral mesh generation for complex geometries remains a challenging problem. Even using IA-Mesh [19], one of the latest developments in hexahedral meshing for biomechanics, an experienced analyst is required to manually adjust the mesh [10]. For example, automatically generated hexahedral elements with the Jacobian less than 0.2 are regarded as of unacceptably poor quality [20, 21] and need to be manually corrected or replaced with tetrahedral elements.

Mesh generation for biological structures remains, after image segmentation, the most tedious and time-consuming step in the application of computational biomechanics. Therefore, automating the modelling workflow represents the most critical challenge in patient-specific biomechanics.

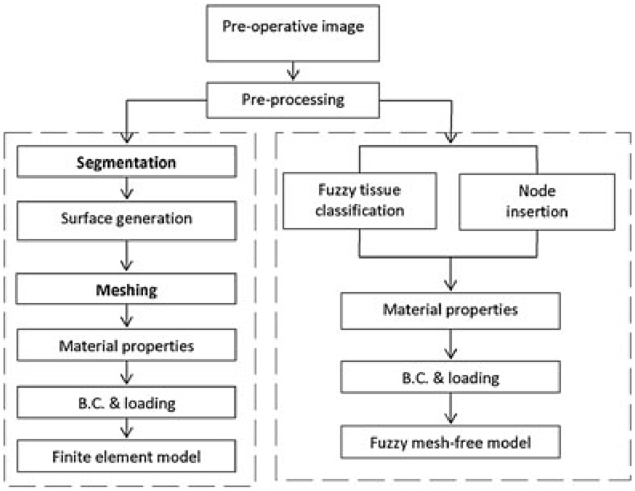

Figure 1. Comparison between conventional finite element biomechanical modelling (left column) and the proposed fuzzy mesh-free modelling (right column).

In the past few years our research group developed a suite of finite element algorithms specifically for simulating large deformations of soft organs, based on the Total Lagrangian formulation and explicit time integration (TLED) [22–24]. While applying these algorithms for patient-specific computations, some critical weakness of the finite element method became evident: the requirement for image segmentation and meshing, and solution difficulties because of very large deformations and discontinuities.

Motivated by the need for simple, automatic computational grid generation for nonlinear (large deformation) patient-specific simulations that can handle possible topology changes that occur during neurosurgical procedures such as retractions, cuts and tissue removal [5], the Intelligent Systems for Medicine Laboratory has been developing a mesh-free Total Lagrangian explicit dynamics (MTLED) method specifically for computing deformation of very soft tissues [25]. The algorithm uses a modified element-free Galerkin method. The deformations are calculated at nodes that are not part of an element mesh. Node placement is almost arbitrary. Fully nonlinear Total Lagrangian formulation is used. Spatial integration is performed over a regular background grid that does not conform to the simulation domain geometry. Explicit time integration is used via the central difference method. The computational results of MTLED are promising; however, the MTLED presented in [25] still requires segmentation, making the modelling procedure a nontrivial task.

In this paper we advance our MTLED framework by avoiding the segmentation procedure in the workflow to fully utilise the merits of mesh-free methods. The idea is to avoid hard segmentation and surface generation but still be able to assign different tissue properties through a fuzzy tissue classification, as shown in Figure 1, right column. Notice that because the classification is fuzzy, we do not generate surfaces. Material properties are directly assigned to the integration points. Although fuzzy tissue classification may slightly impede the accuracy of stress computation, the verification (see Section 5) shows that the overall accuracy is little affected. Most importantly the computational grid becomes more robust and the whole patient-specific modelling workflow is simplified and much easier to automate.

The anatomical data and boundary conditions used in the presented work are extracted from high resolution preoperative and intraoperative magnetic resonance images (MRI) of patients undergoing brain tumour surgery at the Department of Surgery, Brigham and Women's Hospital (Harvard Medical School, Boston, MA, USA).

In the next section we describe our mesh-free solution algorithms. In Section 3, material properties assignment based on fuzzy tissue classification is discussed. Loading and boundary conditions that complete the modelling framework are covered in Section 4. We analyse the performance and accuracy of the proposed framework compared with finite element results obtained using ABAQUS (SIMULIA, Providence, Rhode Island, USA) in Section 5. Section 6 contains the discussion and conclusions.

2. MESH-FREE TOTAL LAGRANGIAN EXPLICIT DYNAMIC ALGORITHM

An overview of the MTLED algorithm is presented in Figure 2 [25]. Specific details are presented in the following sections.

2.1. Geometry discretisation

In MTLED the computational grid for field variable approximation and the background cells for numerical integration are separated over the problem domain.

For field variable approximation, we discretise the simulation domain geometry Ω by nodes where the mass is concentrated, and forces and displacements are calculated.

For nodal reaction force spatial integration, we use a uniform background grid that does not conform to the domain geometry. Numerical integration is performed in each cell using a single-point Gaussian quadrature. Because we do not require the background cell to conform to the intracranial geometry, its generation can be performed automatically (see Figure 3). Previous studies on computing the brain responses under a load similar to ours confirm the accuracy of the approach [26, 27].

DOI: 10.1002/cnm

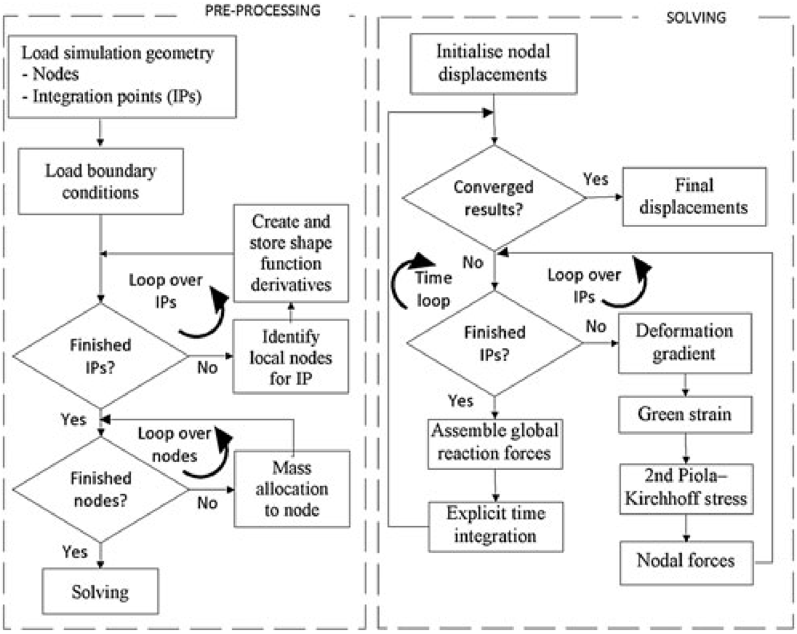

Figure 2. Workflow of mesh-free Total Lagrangian explicit dynamic algorithm.

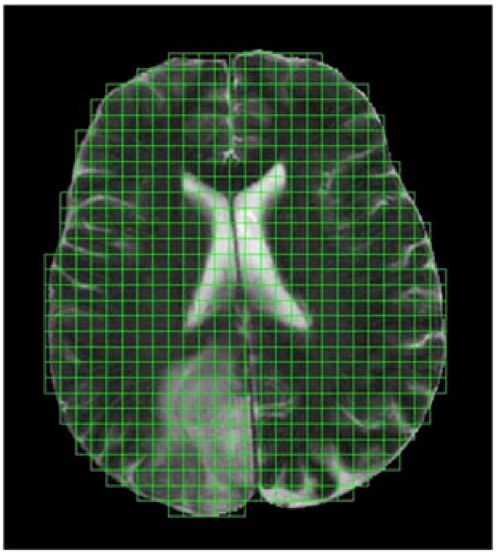

Figure 3. Schematic representation of background integration cells that do not conform to the intracranial geometry.

2.2. *Influence domain*

The influence domain for a node is the bounded region $S \subset \Omega$ that contains all the points whose shape functions are influenced by that node. We use the simplest form of influence domain, which is a sphere with radius r. The value of r is based on factors such as the size of the problem domain Ω, the density of nodes and the required accuracy. All points within this radius are considered to be influenced by the centre node, see Figure 4. The support domain for a point includes all the nodes that have that point in their influence domains — these nodes will be used for shape functions computation at that point.

DOI: 10.1002/cnm

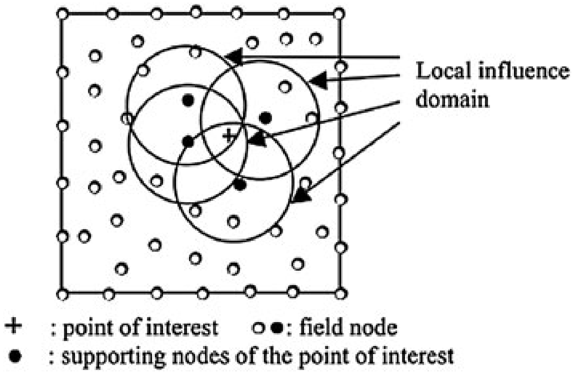

Figure 4. Schematic representation of mesh-free discretisation facilitating arbitrary distribution of nodes.

The construction of influence domains is of critical importance because it is the basis for computing shape functions and their derivatives. If influence domains are too large, too many nodes are included in the support domain of each point, which will influence the approximation accuracy and increase the computation burden. If influence domains are too small and not enough nodes are included in the support domain of a given point, the shape functions computation will become impossible. In [25] we fixed the number of nodes per integration point by modifying the support domains for each integration point. The benefit of that approach is the control over the number of nodes involved in the computation of shape functions, so that the possibility of using either too many or too few nodes per integration point is eliminated. However, because of the different sizes of support domains, the shape functions may not be continuous in the problem domain. This may introduce problems when calculating shape function derivatives or calculating displacements for a point that is not an integration point and can influence the convergence of the solution. In this paper we eliminate the restrictions on the number of nodes per integration point, to ensure the continuity of the shape functions.

2.3. *Shape functions*

In this study, moving-least-squares shape functions are used for their simplicity and robustness. For any point $x \in \Omega$, the field variable $u(x)$ is approximated with $u^h(x)$

$$\begin{aligned} u^h(\mathbf{x}) &= \sum_{j=1}^{m} p_j(\mathbf{x}) a_j(\mathbf{x}) \\ &= \mathbf{p}^T(\mathbf{x})\mathbf{a}(\mathbf{x}) \end{aligned} \tag{1}$$

where m is the number of terms in the vector of basis functions $\mathbf{p}^T(\mathbf{x})$ and $\mathbf{a}(\mathbf{x})$ is an m-vector of unknown shape function coefficients, calculated from the minimization of functional J

$$J(\mathbf{x}) = \sum_{i=1}^{n} \left[(u^h(\mathbf{x}_i) - u_i)^2 \mathrm{w}(\mathbf{x} - \mathbf{x}_i) \right] \tag{2}$$

J represents the difference between the local approximation $u^h(\mathbf{x})$ and the function $u(\mathbf{x})$, n is the number of nodes in the support domain and $\mathrm{w}(\mathbf{x} - \mathbf{x}_i)$ is the quartic spline weight function based on the distance between the nodes $\mathbf{x}_i$ and the centre point $\mathbf{x}$.

We use low-order monomials as basis functions, but it is possible to use more advanced functions in the basis to deal with singularities that may arise in certain problems. It should be noted that, as shown in [28], the moving-least-squares shape functions are not polynomials. More details about the formulation of the shape functions in the context of mesh-free TLED are given in [25].

In MTLED, shape functions and their derivatives are calculated entirely in the preprocessing stage, as shown in Figure 2.

2.4. *Total Lagrangian explicit dynamics*

The fuzzy mesh-free method uses a Total Lagrangian formulation for calculating forces from stresses and displacements. This means all the calculations are referring to the initial configuration of the analysed continuum. The decisive advantage of this formulation is that large amount of computation, such as all derivatives with respect to spatial coordinates, can be carried out during the preprocessing stage. As indicated in [23], the Total Lagrangian formulation significantly reduces the computation time compared with the Updated Lagrangian formulation used in a vast majority of commercial finite element solvers (such as LS-DYNA, ABAQUS). Also the material law implementation is much simpler because hyper-elastic models can be easily described using the deformation gradient.

From [23, 29], the nodal forces are computed as

$$ {}^t_0\mathbf{F} = \int_{V_0} {}^t_0\mathbf{X}{}^t_0\mathbf{S}{}_0\mathbf{B}\,\mathrm{d}V_0 \tag{3}$$

where ${}^t_0\mathbf{X}$ is the deformation gradient at time t, ${}^t_0\mathbf{S}$ is the second Piola–Kirchoff stress and ${}_0\mathbf{B}$ is the matrix of shape function derivatives [25].

We apply explicit integration in time domain using the central difference method. This allows very straightforward treatment of nonlinearities because no iterations are required during each time step. The time stepping scheme for solving the equation of motion can be expressed as

$$ {}^{t+\Delta t}\mathbf{U} = \Delta t^2 \mathbf{M}^{-1}\, {}^t_0\mathbf{F} + 2\,{}^t\mathbf{U} - {}^{t-\Delta t}\mathbf{U} \tag{4}$$

where ${}^t\mathbf{U}$ is the displacement calculated at time t, $\mathbf{F}$ is the reaction force, and $\mathbf{M}$ is the constant lumped mass matrix. The mass associated with an integration point is distributed equally to all nodes found in the support domain of that integration point.

Explicit time integration is only conditionally stable and therefore requires careful selection of maximum stable time step that can be used. We use an estimate of the stable time step derived for the specific mass lumping algorithm for mesh-free methods, as described in [30].

The advantage of using a lumped mass matrix is that the system of equations (4) can be decoupled and the solution is computed separately for each degree of freedom. Therefore, during the whole solution algorithm, the global stiffness matrix for the entire model is not needed and no system of equations must be solved. The computation time can be reduced by an order of magnitude compared with implicit integration [31].

2.5. *Dynamic relaxation*

We use dynamic relaxation [32] in the solution algorithm to allow for very fast and accurate convergence to the deformed state.

In dynamic relaxation, a mass proportional damping component is added to the equation of motion so that Equation (4) becomes

$$ {}^{t+\Delta t}\mathbf{U} = {}^t\mathbf{U} + \alpha({}^t\mathbf{U} - {}^{t-\Delta t}\mathbf{U}) + \beta \mathbf{M}^{-1}\,{}^t_0\mathbf{F} \tag{5}$$

$$ \alpha = \frac{2 - c\Delta t}{2 + c\Delta t} \tag{6}$$

$$ \beta = \frac{2\Delta t^2}{2 + c\Delta t} \tag{7}$$

where c is the damping coefficient.

In the relaxation stage, the integration time step Δt is kept constant, while the damping coefficient c and lumped mass matrix $\mathbf{M}$ are initiated following Ref. [33] and automatically adjusted to maximize the convergence rate and improve the computational efficiency without compromising the solution convergence [33].

During dynamic relaxation we use a termination criteria based on an estimate of the maximum absolute error in the solution instead of residual forces or energy, as commonly used in finite element software. As explained in [32], dynamic relaxation attenuates more strongly the high frequency oscillations so that the calculated displacement will converge towards the real solution at a frequency close to the smallest oscillation frequency. The absolute error vector will also converge towards the eigenvector corresponding to the lowest eigenvalue of the equation of motion. Therefore, the solution error decreases at each step by

$$\mathbf{U}^{n+1} - \mathbf{U}^{*} \approx \rho(\mathbf{U}^{n} - \mathbf{U}^{*}) \tag{8}$$

where ρ is the estimated convergence rate and $\mathbf{U}^*$ is the steady state solution.

The maximum absolute error can be approximated by applying the infinity norm to (8)

$$\begin{aligned} &\left\|\mathbf{U}^{n+1} - \mathbf{U}^{*}\right\|_{\infty} \leqslant \rho\left(\left\|\mathbf{U}^{n+1} - \mathbf{U}^{*}\right\|_{\infty} + \left\|\mathbf{U}^{n+1} - \mathbf{U}^{n}\right\|_{\infty}\right) \quad => \\ &\left\|\mathbf{U}^{n+1} - \mathbf{U}^{*}\right\|_{\infty} \leqslant \frac{\rho}{1-\rho}\left\|\mathbf{U}^{n+1} - \mathbf{U}^{n}\right\|_{\infty} \end{aligned} \tag{9}$$

During dynamic relaxation, if the estimated absolute error (given by the right-hand side of Equation (9)) is smaller than a configured threshold for a consecutive number of steps, we consider the tolerance is satisfied and the simulation is ended. In the current study, following Ref. [33], the termination threshold is set to 0.1 mm and the number of consecutive steps is set to 50.

3. MATERIAL PROPERTIES BASED ON FUZZY TISSUE CLASSIFICATION

In the modelling process, material properties need to be assigned to each integration point based on information from the medical image. Traditional hard segmentation contains less information than the original image because it converts intensity values to discrete label maps. Each tissue class is assigned uniform material properties based on the label map, as shown in Figures 5(b) and (c). On the other hand, fuzzy tissue classification contains the image intensity information in the fuzzy membership functions — see Figures 5(d) and (e). In the present study we use fuzzy tissue classification instead of segmentation in our mesh-free modelling process.

Before we discuss further, we would like to clarify the difference between segmentation and tissue classification. Although interchangeable usage is often seen in the literature, segmentation and tissue classification do have differences in terms of procedures and outcomes. Segmentation partitions an image into nonoverlapping and connected regions with discretely defined boundaries, while tissue classification assigns each pixel (voxel) to a number of different tissue types [34]. Note that the requirement for the regions to be connected is removed so that the classification can be fuzzy (or soft), resulting in fuzzy membership functions for each tissue class rather than discrete label maps. This leads to an easier and more flexible modelling process.

The use of fuzzy tissue classification makes a substantial difference in the modelling workflow. As shown in Figure 5(a), malignant brain tumour can spread within the brain and spine. Lacking distinct borders, tumour is then very difficult to segment, although segmentation is essential in finite element modelling.

There is extensive literature on tissue classification of brain images [35–37]. To cope with extreme and variable anatomies because of pathologies, we developed a simple yet efficient semi-automatic fuzzy tissue classification method based on fuzzy C-Mean (FCM) clustering [38]. FCM clusters similar intensity data by computing the membership function at each pixel for a specified number of classes C and minimising the objective function J_{FCM}.

$$J_{\mathrm{FCM}} = \sum_{j \in \Omega} \sum_{k=1}^{C} u_{jk} \left\| I_j - V_k \right\| \tag{10}$$

$$0 \leqslant u_{jk} \leqslant 1, \sum_{k=1}^{C} u_{jk} = 1 \tag{11}$$

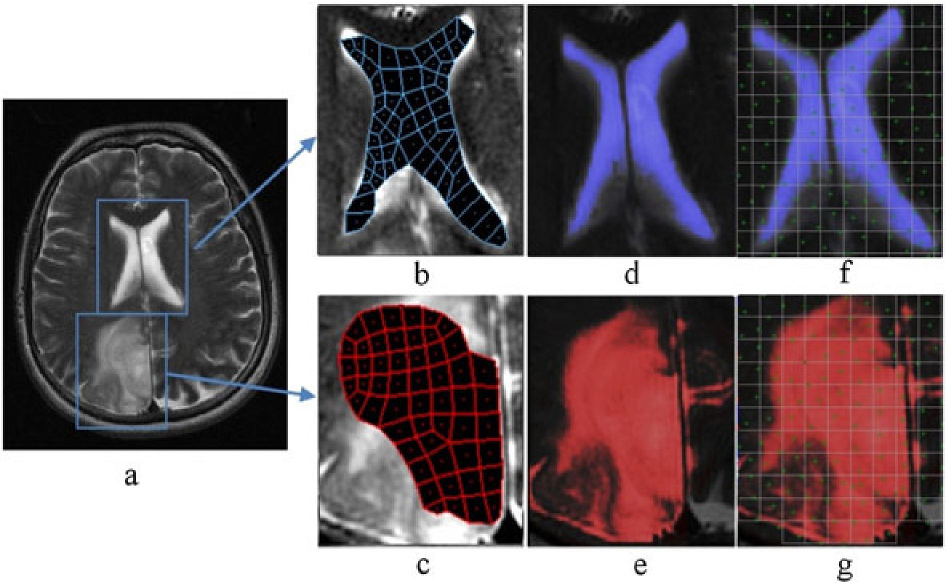

Figure 5. Comparison between a finite element model constructed using segmentation and a fuzzy mesh-free model based on fuzzy tissue classification. (a) T2 MRI of the brain, including the tumour and ventricles — notice that no clear boundaries can be easily defined, especially for the tumour; (b) finite element model of ventricles generated from segmentation; (c) finite element model of the tumour generated from segmentation; (d) the fuzzy membership function for ventricle indicated at each pixel by the level of blue; (e) the fuzzy membership function for tumour indicated at each pixel by the level of red; (f) fuzzy mesh-free model of ventricle; and (g) fuzzy mesh-free model of tumour. Green dots represent nodes while grey grids define the background integration cells. Material properties are assigned directly to integration points based on the fuzzy classification results.

where Ω is the image domain; j is the location index; k is the class index; and $I_j - V_k$ represents the degree of similarity between the intensity I at that location j and the centroid of its class V_k. Notice that the fuzzy membership u_{jk} will form a partition of unity for different classes. A high membership value means that the data value at that location is close to the centroid for that particular class. Our mesh-free model contains three tissue classes ($C = 3$): healthy tissue (as the same properties for white and gray matter are used without introducing noticeable errors in computed displacements [10]), ventricles and tumour.

Continuous material properties MP_j at each location j are interpolated based on these membership functions from FCM as follows:

$$MP_j = \sum_{k=1}^{C} u_{jk} \times MP_k \tag{12}$$

Despite continuing efforts [39, 40], commonly accepted noninvasive methods for determining patient-specific constitutive properties of the brain have not been developed yet. In the context of brain biomechanics for nonrigid registration, constitutive models of brain tissue vary from simple linear-elastic models [41] to Ogden hyperelastic models [31] and biphasic models based on consolidation theory [42]. However, because of the strength of the modelling approach used in this study (explained in Section 4.1), the calculated brain deformation depends very weakly on the constitutive model and mechanical properties of the brain tissues. Therefore, following [10, 22, 32], we use the hyper-elastic Neo-Hookean model. The literature indicates that hyper-elastic models capture well the behaviour of brain tissues undergoing large deformation [6]. The Neo-Hookean model is chosen for its simplicity, which is essential for large-scale real-time simulation.

We use the same form of Neo-Hookean strain energy potential as the one in ABAQUS

$$U = \frac{\mu_0}{2}\left(\overline{I}_1 - 3\right) + \frac{k_0}{2}(J-1)^2 \tag{13}$$

where μ_0 is the initial shear modulus, k_0 is the initial bulk modulus, $\overline{I}_1$ is the first deviatoric strain invariant, and J is the volumetric change.

On the basis of the experimental data [43] and prior modelling experience [44], the Young's modulus is set to 3000 Pa for the brain parenchyma tissue and 6000 Pa for the tumour. There is strong experimental evidence [6, 45] that the brain tissue is (almost) incompressible; therefore, we assign a Poisson's ratio of 0.49 for parenchyma and tumour. Following Refs. [10, 31] the ventricles are set to be very soft and compressible — we set Young's modulus to 10 Pa and Poisson's ratio to 0.1 (to account for the possible leakage of cerebrospinal fluid from ventricles during surgery).

In the fuzzy mesh-free TLED model, material properties (Young's modulus and Poisson's ratio) are assigned directly to each Gauss (integration) point based on nearest-neighbour correspondence. More complicated assignment schemes can be defined (such as averaging of properties over the integration cell), but in this work we used the simpler nearest-neighbour approach.

4. LOADING AND BOUNDARY CONDITIONS

Accurate quantification and modelling of load and boundary conditions, which complete the patient-specific modelling process, are critical for biomechanical simulations.

4.1. Displacement–zero traction loading

The exact physiological mechanisms behind the craniotomy-induced brain shift are hotly disputed in the neurosurgical community and require further studies [46]. Furthermore, there are always uncertainties in the patient-specific properties of tissues.

To reduce the effects of such uncertainties, in the present study, craniotomy-induced brain shift is modelled as a 'displacement–zero traction' problem [5, 6]. The model is loaded by enforced displacement of the nodes found on the brain surface exposed by craniotomy (Figure 6). Such information can be measured using a variety of techniques, such as laser range scanning [47]. In the present study the displacements for loading are given by the distances between corresponding points on the preoperative and intraoperative cortical surfaces. The correspondence between these surfaces is determined by applying a B-spline registration algorithm to their curvature maps [48].

4.2. Brain–skull interaction

We model the interaction between skull and brain as a finite sliding, frictionless contact. Because the skull is orders of magnitude stiffer than the brain tissue, we assume the skull to be rigid. A contact interface is defined between the rigid skull and the brain surface. The contact formulation

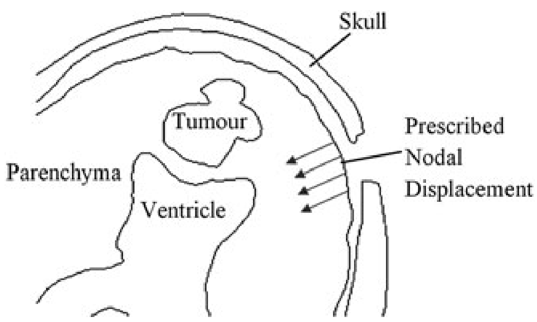

Figure 6. Model loading through enforced displacement of the nodes found on the brain surface in the craniotomy area. The prescribed motion of the boundary is represented by arrows.

DOI: 10.1002/cnm

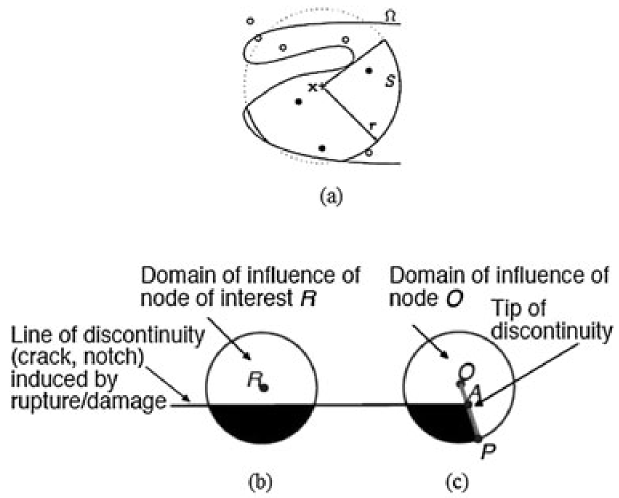

Figure 7. Nonconvex boundaries (a) and visibility criterion (b, c).

described in [22, 49] is used, which detects and prevents the penetration of the skull by any brain nodes while allowing frictionless sliding. Such modelling, although simple, has been used in the literature [10, 50] for computing brain deformations during brain shift because of its reliability and low computational cost.

4.3. Modelling of nonconvex geometry using visibility criterion

In the case of brain modelling, the complexity of tissue structure leads to a nonconvex brain boundary, which means that some nodes are geometrically close but are not coupled mechanically.

In the present study, such nonconvex boundaries are modelled by modifying the shape functions using the visibility criterion [28] to reflect the fact that nodes and integration points located on the opposite sides of the discontinuities cannot influence each other. The discontinuity is considered opaque, which implies that if a line from a point in space to a node is treated as a ray of light and the ray encounters the (opaque) discontinuity, the point is not included in the node's influence domain. The concept of visibility criterion is shown in Figures 7(b) and (c) by the altered support domain of nodes R and O adjacent to a line of discontinuity. Points in the shaded region are removed from domains of influence.

5. RESULTS

To evaluate the performance of the proposed model, we compare the fuzzy mesh-free simulation results against finite element results computed using ABAQUS for three cases of craniotomy-induced brain shift. The three cases are chosen to represent different situations that may occur during neurosurgery as characterised by tumours located in different parts of the brain, as shown in Figure 8. Images were provided by the Computational Radiology Laboratory (Children's Hospital; Harvard Medical School, Boston, MA).

The finite element meshes (as shown in Figure 9, left column) are constructed from the segmented preoperative MRIs. We use standard linear quadrilateral plain strain elements. All elements are explicitly classified into three different tissue types: parenchyma (white), tumour (red) and ventricle (blue). To allow deformations to propagate between the parenchyma, tumour and ventricles, shared nodes are used between different tissues. This ties the surfaces of different tissues together without needing to define any extra internal boundary conditions. The meshes are generated using Hypermesh (a high-performance commercial finite element mesh generator by Altair, Ltd. of Troy, MI, USA) with local manual adjustments.

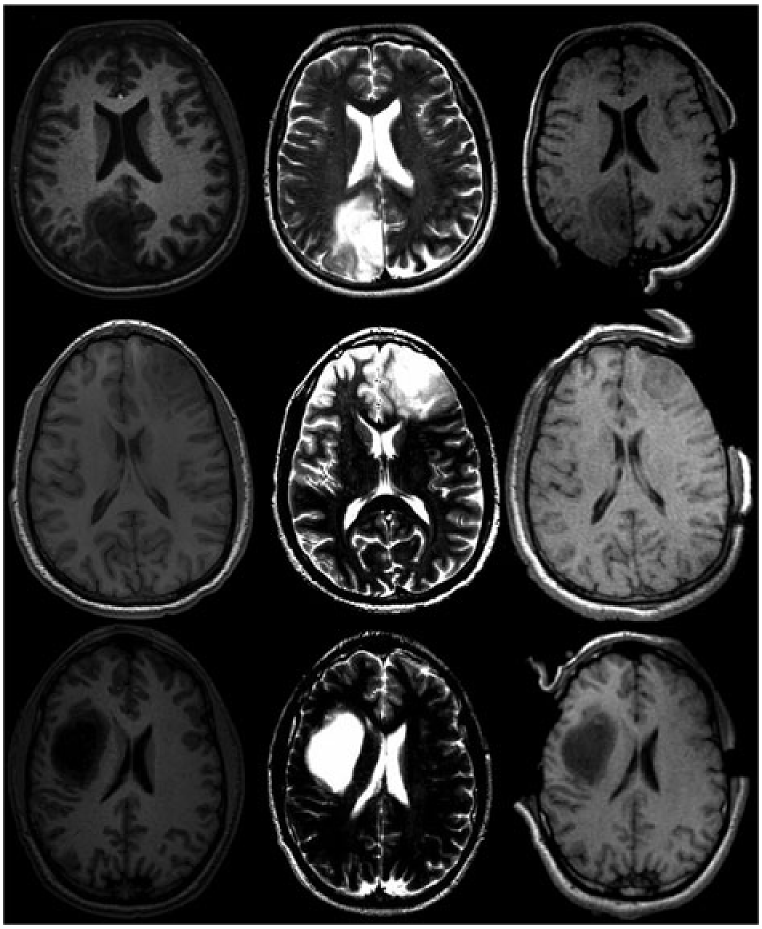

Figure 8. Three cases selected for demonstration and evaluation, T1 preoperative MRI (left column), T2 preoperative MRI (middle column) and intraoperative MRI showing craniotomy area (right column). The MRIs were provided by Computational Radiology Laboratory, Harvard Medical School.

The fuzzy mesh-free models are shown in Figure 9 (middle column). The levels of red and blue in the image correspond to the values of the membership functions for tumour and ventricles as generated by the fuzzy tissue classification algorithm. Nodes are represented by green dots in the domain. Compared with the finite element model, the information contained in the fuzzy mesh-free model is much richer. Uncertainties about tissue classes are included in the numerical simulation. However, unlike creation of finite element meshes, generation of fuzzy mesh-free models is a trivial exercise.

For both finite element and fuzzy mesh-free models, we use the same constitutive material laws (as described in Section 3), loading (Section 4.1) and boundary conditions (Section 4.2).

H-refinement of mesh density is used for all three cases to obtain a converged control solution for the finite element model solved by ABAQUS, as shown in Table I. We use approximately the same number of integration cells (corresponding to the number of elements used in ABAQUS) in the fuzzy mesh-free model.

To ensure fast and accurate convergence of our explicit solution method, we use dynamic relaxation as described in Section 2.5. The maximum displacement variations for each time step are shown in Figure 10.

The differences in computed deformation fields from the two models over the whole problem domain are shown in the right column of Figure 9. For each node in the finite element model, the displacements are compared with the displacements at the corresponding position in the fuzzy

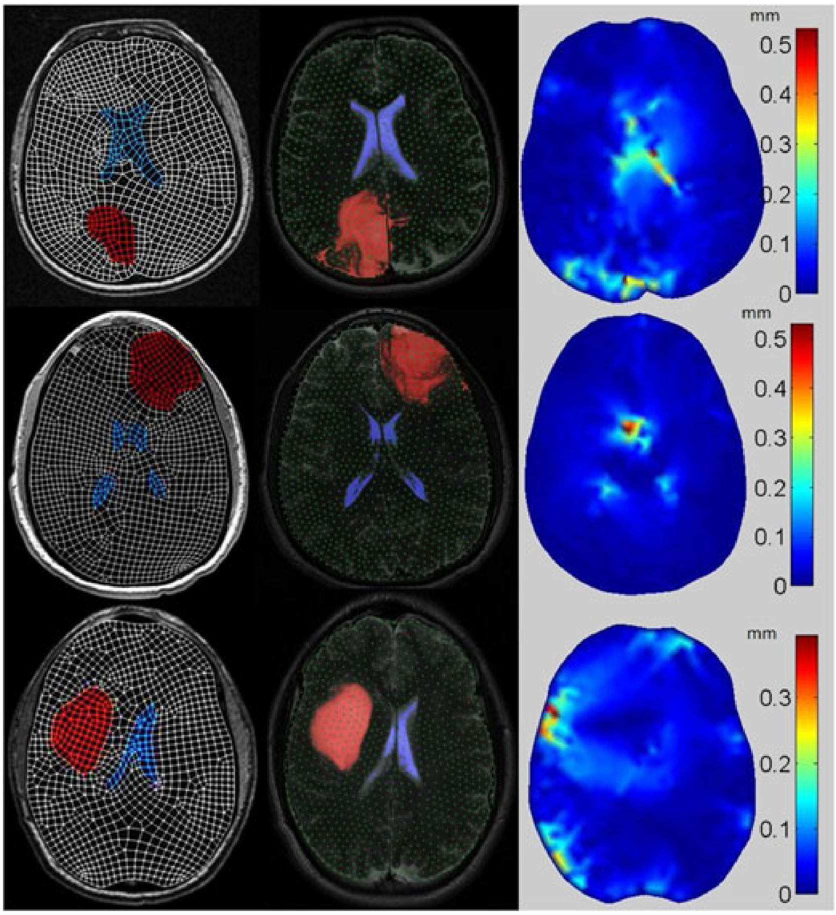

Figure 9. Evaluation of accuracy for three cases. Left column: finite element models, with parenchyma, tumour (red) and ventricle (blue) modelled separately. Middle column: fuzzy mesh-free model without explicitly separating the tumour and ventricles; the fuzzy membership functions are indicated by the level of red for tumour and blue for ventricles; nodes are shown as green dots. Right column: Difference of the simulation results (computed deformation field) from the two models over the whole problem domain [mm].

Table I. Results of H-refinement of mesh density in ABAQUS.

		Case 1		
Number of elements	261	1059	4107	14985
Strain energy [J]	0.033	0.031	0.031	0.031
		Case 2		
Number of elements	301	1120	4315	16283
Strain energy [J]	0.038	0.036	0.036	0.036
		Case 3		
Number of elements	281	1033	3978	15137
Strain energy [J]	0.061	0.053	0.053	0.053

mesh-free model using the approximation scheme introduced in Section 2.3. The maximum and average differences for the three cases are shown in Table II. Because the accuracy of manual neurosurgery is not better than 1 mm [51] and the voxel size in high-quality preoperative magnetic resonance images is usually of a similar magnitude, we can conclude that the difference is,

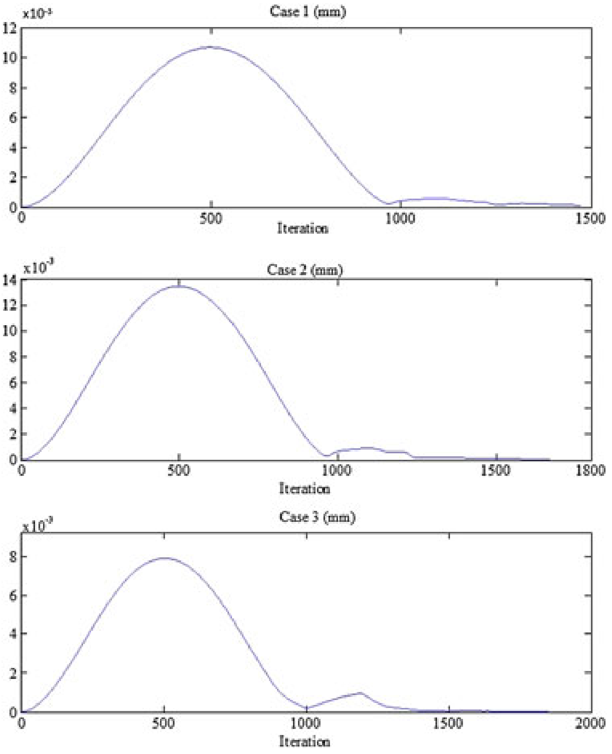

Figure 10. Maximum displacements variation in a time step versus step number when using dynamic relaxation for the three cases analysed. All cases converge to the static solution (shown as almost zero displacements variation) within 2000 time steps.

Table II. Numerical details of comparison for the cases presented in Figure 9.

Case	Nodes (FEM)	Elements (FEM)	Nodes (mesh-free)	Integration points (mesh-free)	Maximum boundary loading [mm]	Average difference [mm]	Maximum difference [mm]
1 (Top)	1117	1059	755	982	5.75	0.0481	0.5719
2 (Middle)	1180	1120	813	1117	7.38	0.0154	0.3827
3 (Bottom)	1095	1033	867	1162	4.87	0.0264	0.5356

for practical purposes, negligible, and therefore the proposed mesh-free models ensure equivalent accuracy to the finite element models.

6. CONCLUSIONS AND DISCUSSION

We introduced a new fuzzy mesh-free framework for modelling brain biomechanics for patient-specific applications. Patient-specific modelling relies on the ability to convert and integrate data from several data sources. For brain biomechanics, the integration of anatomical geometric data, material properties and boundary conditions is of primary importance. In the present work, we extracted material properties directly from fuzzy tissue classification and integrated them with computational grids in a mesh-free framework so that image segmentation and mesh generation are avoided.

The ability to use fuzzy tissue material properties, even with possible local misclassifications, directly in our mesh-free simulation is based on our formulation of computational mechanics problems in such a way that the results are weakly sensitive to the variation in mechanical properties of simulated continua.

DOI: 10.1002/cnm

The difficulties of obtaining patient-specific mechanical properties of soft tissues has stimulated a lot of research in experimental mechanics, from the development of MR and ultrasound elastography [52–54] to renewed interest in inverse problems [55, 56] and *in vivo* mechanical solicitation [57]. Despite recent progress, the *in vivo* properties of human soft tissue are still hard to obtain [6, 43]. Compared with the existing approaches to obtain accurate patient-specific mechanical properties of soft tissue, our fuzzy mesh-free model that is weakly sensitive to uncertainties in mechanical properties is more likely to bear fruit in the near future.

The fuzzy mesh-free modelling approach offers a prospect of using a neuroimage as a biomechanical model. The verification shows that acceptable accuracy of the computed deformation field can be obtained, even if nodes and integration points do not conform to tissue boundaries. Because our solution method is inherently data-parallel (all degrees of freedom are treated in exactly the same way), Graphics Processing Unit (GPU) implementation will allow very high efficiency and a possibility for near-real time intraoperative computations in three dimensions [44, 58].

ACKNOWLEDGEMENTS

The first author was an SIRF scholar at the University of Western Australia during the completion of this research. The financial support of National Health and Medical Research Council (Grant No. 1006031) and Australian Research Council (Grant No. DP1092893 and DP120100402) is gratefully acknowledged.

REFERENCES

1. Warfield SK, Haker SJ, Talos F, Kemper CA, Weisenfeld N, Mewes AUJ, Goldberg-Zimring D, Zou KH, Westin CF, Wells WM, Tempany CMC, Golby A, Black PM, Jolesz FA, Kikinis R. Capturing intraoperative deformations: research experience at Brigham and women's hospital. *Medical Image Analysis* 2005; **9**(2):145–162.
2. Roberts DW, Hartov A, Kennedy FE, Miga MI, Paulsen KD. Intraoperative brain shift and deformation: A quantitative analysis of cortical displacement in 28 cases. *Neurosurgery* 1998; **43**:749–758.
3. Steinmeier R, Fahlbusch R, Ganslandt O, Nimsky C, Buchfelder M, Kaus M, Heigl T, Lenz G, Kuth R, Huk W. Intraoperative magnetic resonance imaging with the magnetom open scanner: concepts, neurosurgical indications, and procedures: a preliminary report. *Neurosurgery* 1998; **43**(4):739–747.
4. Miller K, Wittek A, Joldes GR. Biomechanical modelling of the brain for computer-assisted neurosurgery. In *Biomechanics of the Brain*, Miller K (ed.). Springer: New York, 2011; 111–136.
5. Miller K, Wittek A, Joldes G, Horton A, Dutta-Roy T, Berger J, Morriss L. Modelling brain deformations for computer-integrated neurosurgery. *International Journal for Numerical Methods in Biomedical Engineering* 2010; **26**(1):117–138.
6. Miller K. *Biomechanics of the Brain*. Springer: New York, 2011.
7. Neal ML, Kerckhoffs R. Current progress in patient-specific modeling. *Briefings in Bioinformatics* 2010; **11**(1):111–126.
8. Balafar MA, Ramli AR, Saripan MI, Mashohor S. Review of brain MRI image segmentation methods. *Artificial Intelligence Review* 2010; **33**(3):261–274.
9. Zhang Y, Brady M, Smith S. Segmentation of brain MR images through a hidden Markov random field model and the expectation-maximization algorithm. *IEEE Transactions on Medical Imaging* 2001; **20**(1):45–57.
10. Wittek A, Joldes G, Couton M, Warfield SK, Miller K. Patient-specific non-linear finite element modelling for predicting soft organ deformation in real-time; Application to non-rigid neuroimage registration. *Progress in Biophysics and Molecular Biology* 2010; **103**(2-3):292–303.
11. Shewchuk JR. Delaunay refinement algorithms for triangular mesh generation. *Computational Geometry: Theory and Applications* 2002; **22**(1-3):21–74.
12. Carey GF. *Computational Grid: Generation, Adaptation, and Solution Strategies*. Taylor& Francis: London, 1997.
13. Lorensen WE, Cline HE. Marching cubes: a high resolution 3d surface construction algorithm. *Computer Graphics (ACM)* 1987; **21**(4):163–169.
14. Viceconti M, Taddei F. Automatic generation of finite element meshes from computed tomography data. *Critical Reviews in Biomedical Engineering* 2003; **31**(1):27–72.
15. Zienkiewicz OC, Rojek J, Taylor RL, Pastor M. Triangles and tetrahedra in explicit dynamic codes for solids. *International Journal for Numerical Methods in Engineering* 1998; **43**(3):565–583.
16. Joldes GR, Wittek A, Miller K. Non-locking tetrahedral finite element for surgical simulation. *Communications in Numerical Methods in Engineering* 2009; **25**(7):827–836.
17. Miller K, Chinzei K. Constitutive modeling of brain tissue: Experiment and theory. *Journal of Biomechanics* 1997; **30**(11/12):1115–1121.
18. Miller K, Chinzei K. Mechanical properties of brain tissue in tension. *Journal of Biomechanics* 2002; **35**:483–490.

19. Grosland NM, Shivanna KH, Magnotta VA, Kallemeyn NA, DeVries NA, Tadepalli SC, Lisle C. IA-FEMesh: An open-source, interactive, multiblock approach to anatomic finite element model development. *Computer Methods and Programs in Biomedicine* 2009; **94**:96–107.
20. Ito Y, Shih AM, Soni BK. Octree-based reasonable-quality hexahedral mesh generation using a new set of refinement templates. *International Journal for Numerical Methods in Engineering* 2009; **77**(13):1809–1833.
21. Shepherd J, Johnson C. Hexahedral mesh generation for biomedical models in SCIRun. *Engineering with Computers* 2009; **25**(1):97–114.
22. Joldes GR, Wittek A, Miller K. Suite of finite element algorithms for accurate computation of soft tissue deformation for surgical simulation. *Medical Image Analysis* 2009; **13**(6):912–919.
23. Miller K, Joldes G, Wittek A. Total Lagrangian explicit dynamics finite element algorithm for computing soft tissue deformation. *Communications in Numerical Methods in Engineering* 2007; **23**(2):121–134.
24. Wittek A, Joldes G, Miller K. Algorithms for Computational Biomechanics of the Brain. In *Biomechanics of the Brain*, Miller K (ed.). Springer: New York, 2011; 189–219.
25. Horton A, Wittek A, Joldes GR, Miller K. A meshless total Lagrangian explicit dynamics algorithm for surgical simulation. *International Journal for Numerical Methods in Biomedical Engineering* 2010; **26**(8):977–998.
26. Horton A, Wittek A, Miller K. Towards meshless methods for surgical simulation. *Computational Biomechanics for Medicine Workshop, Medical Image Computing and Computer-Assisted Intervention MICCAI*, Copenhagen, Denmark, 2006; 34–42.
27. Horton A, Wittek A, Miller K. Subject-specific biomechanical simulation of brain indentation using a meshless method. *International Conference on Medical Image Computing and Computer-Assisted Intervention MICCAI*, Brisbane, Australia, 2007; 541–548.
28. Belytschko T. Meshless methods: an overview and recent developments. *Computer Methods in Applied Mechanics and Engineering* 1996; **139**(1-4):3–47.
29. Bathe K-J. *Finite Element Procedures*. Prentice-Hall: New Jersey, 1996.
30. Joldes GR, Wittek A, Miller K. Stable time step estimates for mesh-free particle methods. *International Journal for Numerical Methods in Engineering* 2012; **91**(4):450–456. DOI: 10.1002/nme.4290.
31. Wittek A, Miller K, Kikinis R, Warfield S. Patient-specific model of brain deformation: Application to medical image registration. *Journal of Biomechanics* 2007; **40**(4):919–929.
32. Joldes GR, Wittek A, Miller K. Computation of intra-operative brain shift using dynamic relaxation. *Computer Methods in Applied Mechanics and Engineering* 2009; **198**(41-44):3313–3320.
33. Joldes GR, Wittek A, Miller K. An adaptive dynamic relaxation method for solving nonlinear finite element problems. Application to brain shift estimation. *International Journal for Numerical Methods in Biomedical Engineering* 2011; **27**(2):173–185.
34. Pham DL. Current methods in medical image segmentation. *Annual Review of Biomedical Engineering* 2000; **2**(1):315–337.
35. Lin GC, Wang WJ, Kang CC, Wang CM. Multispectral MR images segmentation based on fuzzy knowledge and modified seeded region growing. *Magnetic Resonance Imaging* 2012; **30**(2):230–246.
36. Weisenfeld NI, Warfield SK. Learning likelihoods for labeling (L3): a general multi-classifier segmentation algorithm. *International Conference on Medical Image Computing and Computer-Assisted Intervention MICCAI*, Toronto, Canada, 2011; 322–329.
37. Wells WM, Crimson WEL, Kikinis R, Jolesz F. Adaptive segmentation of mri data. *IEEE Transactions on Medical Imaging* 1996; **15**(4):429–442.
38. Pham DL, Prince JL. Adaptive fuzzy segmentation of magnetic resonance images. *Medical Imaging, IEEE Transactions on* 1999; **18**(9):737–752.
39. Sinkus R, Tanter M, Xydeas T, Catheline S, Bercoff J, Fink M. Viscoelastic shear properties of in vivo breast lesions measured by MR elastography. *Magnetic Resonance Imaging* 2005; **23**:159–165.
40. Turgay E, Salcudean S, Rohling R. Identifying the mechanical properties of tissue by ultrasound strain imaging. *Ultrasound in Medicine and Biology* 2006; **32**(2):221–235.
41. Warfield SK, Ferrant M, Gallez X, Nabavi A, Jolesz FA, Kikinis R. Real-time biomechanical simulation of volumetric brain deformation for image guided neurosurgery. *SC 2000: High Performance Networking and Computing Conference*, Dallas, USA, 2000; 1–16.
42. Miga MI, Paulsen KD, Hoopes PJ, Kennedy FE, Hartov A, Roberts DW. In vivo modeling of interstitial pressure in the brain under surgical load using finite elements. *Transactions of the ASME. Journal of Biomechanical Engineering* 2000; **122**(4):354–363.
43. Miller K, Chinzei K, Orssengo G, Bednarz P. Mechanical properties of brain tissue in-vivo: Experiment and computer simulation. *Journal of Biomechanics* 2000; **33**(11):1369–1376.
44. Joldes G, Wittek A, Couton M, Warfield S, Miller K. Real-time prediction of brain shift using nonlinear finite element algorithms. *Medical Image Computing and Computer-Assisted Intervention MICCAI*, London, UK, 2009; 300–307.
45. Sahay KB, Mehrotra R, Sachdeva U, Banerji A. Elastomechanical characterization of brain tissues. *Journal of Biomechanics* 1992; **25**(3):319–326.
46. Aarabi B, Hesdorffer DC, Ahn ES, Aresco C, Scalea TM, Eisenberg HM. Outcome following decompressive craniectomy for malignant swelling due to severe head injury. *Journal of Neurosurgery* 2006; **104**(4):469–479.
47. Miga MI, Sinha TK, Cash DM, Galloway RL, Weil RJ. Cortical surface registration for image-guided neurosurgery using laser-range scanning. *IEEE Transactions on Medical Imaging* 2003; **22**(8):973–985.

48. Joldes GR, Wittek A, Miller K. Cortical surface motion estimation for brain shift prediction. *Computational Biomechanics for Medicine IV Workshop, MICCAI*, London, UK, 2009; 50–59.
49. Joldes GR, Wittek A, Miller K, Morriss L. Realistic and efficient brain-skull interaction model for brain shift computation. *Computational Biomechanics for Medicine III Workshop, MICCAI*, New-York, 2008; 95–105.
50. Miller K, Wittek A, Joldes G, Ma J, Zwick BJ. Computational biomechanics of the brain; application to neuroimage registration. In *Neural Tissue Biomechanics*, Bilston LE (ed.). Springer: Berlin Heidelberg, 2011; 135–157.
51. Bucholz R, MacNeil W, McDurmont L. The operating room of the future. *Clinical Neurosurgery* 2004; **51**:228–237.
52. Muthupillai R, Lomas D, Rossman P, Greenleaf J, Manduca A, Ehman R. Magnetic resonance elastography by direct visualization of propagating acoustic strain waves. *Science* 1995; **269**(5232):1854–1857.
53. Sarvazyan AP, Rudenko OV, Swanson SD, Fowlkes JB, Emelianov SY. Shear wave elasticity imaging: a new ultrasonic technology of medical diagnostics. *Ultrasound in Medicine & Biology* 1998; **24**(9):1419–1435.
54. Xu L, Lin Y, Han JC, Xi ZN, Shen H, Gao PY. Magnetic resonance elastography of brain tumors: preliminary results. *Acta Radiologica* 2007; **48**(3):327–330.
55. Gee MW, Förster C, Wall WA. A computational strategy for prestressing patient-specific biomechanical problems under finite deformation. *International Journal for Numerical Methods in Biomedical Engineering* 2010; **26**(1):52–72.
56. Sinkus R, Daire J-L, Van Beers BE, Vilgrain V. Elasticity reconstruction: Beyond the assumption of local homogeneity. *Comptes Rendus Mécanique* 2010; **338**(7–8):474–479.
57. Schiavone P, Chassat F, Boudou T, Promayon E, Valdivia F, Payan Y. In vivo measurement of human brain elasticity using a light aspiration device. *Medical Image Analysis* 2009; **13**(4):673–678.
58. Joldes GR, Wittek A, Miller K. Real-time nonlinear finite element computations on GPU - application to neurosurgical simulation. *Computer Methods in Applied Mechanics and Engineering* 2010; **199**(49-52):3305–3314.

DOI: 10.1002/cnm